

See discussions, stats, and author profiles for this publication at: <https://www.researchgate.net/publication/316239920>

The Impact of Tandem Rotor Blades on the Performance of Transonic Axial Compressors

Article in *Aerospace Science and Technology* · April 2017

DOI: 10.1016/j.ast.2017.04.019

CITATIONS

47

READS

2,325

3 authors, including:



Mohamed Mohsen Ahmed
University of Maryland, College Park

17 PUBLICATIONS 145 CITATIONS

[SEE PROFILE](#)



Farouk Owis
40 PUBLICATIONS 318 CITATIONS

[SEE PROFILE](#)



The impact of tandem rotor blades on the performance of transonic axial compressors

Mohamed Mohsen*, Farouk M. Owis, Ali A. Hashim

Aerospace Engineering Department, Faculty of Engineering, Cairo University, Giza, Egypt



ARTICLE INFO

Article history:

Received 2 August 2016

Received in revised form 12 March 2017

Accepted 9 April 2017

Available online 18 April 2017

Keywords:

Tandem cascades

Off-design

Numerical simulation

ABSTRACT

A numerical investigation has been undertaken to evaluate the potential of tandem rotor blades in improving the overall performance of transonic compressors. This study aims to address guidelines for the design of tandem rotor blades and to provide insights into the flow field in the transonic regime. A tandem rotor design with same inflow characteristics of the reference transonic rotor 'NASA Rotor 37' is proposed. A parametric study based on two-dimensional numerical simulations is performed at the rotor mid-span section with supersonic inlet Mach number of 1.4 to select the suitable design parameters for the three-dimensional computations. Then the tandem rotor performance at design and off-design conditions is examined. The results are compared with the numerical and experimental results of the reference 'NASA Rotor 37'. The numerical results reveal that large improvements in the flow turning and diffusion are obtained without flow separation. The tandem design has a 17% increase in the total pressure ratio and 2% increase in the rotor adiabatic efficiency relative to the baseline rotor 'NASA Rotor 37'.

© 2017 Elsevier Masson SAS. All rights reserved.

1. Introduction

Multi-stage axial flow compressors are the principal type of compressors used in gas turbine engines due to their high efficiency and high flow capacity per unit frontal area. However, the compressor weight is considered the largest among all other components in the gas turbine engine. Manufacturers are always seeking to develop engines with high thrust to weight ratio. This can be accomplished by increasing the single stage total pressure ratio and reducing the number of stages.

To increase the total pressure ratio of a single stage axial flow compressor, there is a challenge of increasing line sweeping and leaning, vortex generators, splitter vanes, slotted blades, tandem blades and counter rotating blades flow turning and diffusion without boundary layer separation. Moreover, in highly loaded transonic axial compressors, the flow diffusion is dependent upon decelerating the flow through a shock system and the flow turning capability is limited by boundary layer separation due to high compressibility effects and the shock-boundary layer interaction.

Several studies are being carried out on the advanced designs of axial flow compressor. Some of them are biased towards the design of advanced blade profile and blade stacking. Other ap-

proaches are concentrated on the compressor casing treatment by means of slots and grooves, and the tip injection or bleeding [1,2].

One way to overcome the separation problem is replacing single blade with two tandem blades, as shown in Fig. 1, such that a fresh boundary layer is created on the rear blade through the gap flow from the front blade pressure side. The theory of tandem rotors is basically extracted from the flap or slat introduction to a conventional aircraft wing to increase its camber to get higher lift without flow separation. Previous studies [3–10] have shown that tandem blades outperform conventional blades in terms of higher diffusion and turning capabilities with lower losses. However, most of these studies concentrated on subsonic shock-free regime.

Experimental studies on two-dimensional subsonic tandem cascades indicate to the advantages of using tandem cascades in terms of increasing the flow turning with less flow separation [3–5]. A further investigation has been carried out by Bammert and Beelte [6]. The researchers performed a rig test on a five stages subsonic compressor. The first and last rotors are single bladed while the other three rotors are tandem and all stators are single bladed. They concluded that the tandem compressor operation didn't raise any problems except a narrow stability range.

More recently, McGlumphy et al. [7,8] performed 2D and 3D numerical simulations on different tandem cascades with NACA-65 airfoil series at subsonic speed. They found that the tandem design is very sensitive to the relative position between the two airfoils. They concluded that the tandem design has the capability to re-

* Corresponding author.

E-mail address: mo.mohsen@cu.edu.eg (M. Mohsen).

Nomenclature

AOR	Axial overlap ratio	γ	Gas constant
CFD	Computational fluid dynamics	ξ	Stagger angle
C	Absolute velocity	σ	Rotor solidity
DF	Diffusion factor	π	Total pressure ratio
EXP	Experimental data	τ	Total temperature ratio
MUSCL	Monotonic Upstream-Centered Scheme for Conservation Laws	ω	Pressure loss coefficient
P	Pressure		
PS	Pressure surface		
SS	Suction surface		
T	Temperature		
TOR	Tangential overlap ratio		
W	Relative velocity		
y^+	Normalized wall distance		
B	Relative flow angle		

<i>Subscripts</i>	
1	Rotor inlet
2	Rotor exit
$t, 1$	Total conditions at station 1
$t, 4$	Total conditions at station 4
t, rel	Total relative conditions
θ	Tangential component

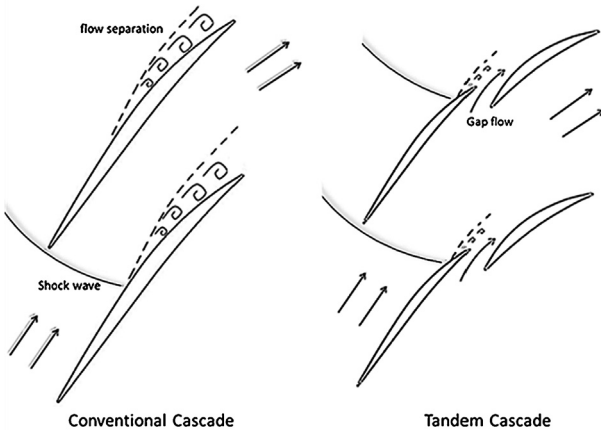


Fig. 1. Layout of conventional and tandem cascades.

place three conventional rotors with two tandem rotors. Hoeger et al. [9,10] conducted 2D experimental and numerical simulations on a developed subsonic tandem cascade at design and off-design conditions. The results of the tandem cascade are compared with those of the conventional cascades of same inlet Mach number and turning. The off-design results showed advantages of the tandem cascade at higher Mach numbers and disadvantages at lower Mach numbers.

In transonic regime, the only work on tandem rotors found in literature was carried out by Hasegawa et al. [11]. They developed a transonic tandem fan for an Air Turbo Ramjet (ATR) engine. The fan testing showed that a pressure ratio of 2.2 could be achieved in a single stage. However, details about the design and analysis of the flow physics at different operating conditions were not presented in details. Other work in transonic regime was performed on stator guide vanes [12,13] with inlet Mach number of 1.06 and 1.25 respectively. This work is focused on the design and performance of stationary tandem blades in which the flow physics is simple compared to rotating blades.

The effect of tandem blades on subsonic compressor performance has been investigated by several researchers. However, the supersonic or transonic flow fields over tandem blades exhibit complicated phenomena such as the shock wave interaction with the gap between the blades. The effect of the shock location on the performance of the tandem blades needs more investigation. Thus, the current study aims at developing an advanced transonic tandem rotor that can benefit from the flow diffusion through a shock system and the large flow turning angle. The simulation of

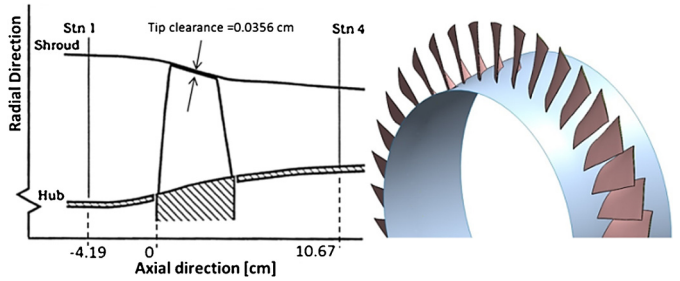


Fig. 2. NASA Rotor 37 geometry.

such flow with a shock system requires special treatment of the numerical mesh in order to resolve accurately the flow field near the shock without producing large numerical oscillations. As the flow conditions or the blade shape are being changed during the current study the shock position changes over the blade. Thus, the grids used in the numerical simulations need to be modified carefully.

The inflow characteristics are kept similar to those in the reference rotor NASA Rotor 37 to be able to provide a comparison between their performance at design and off-design conditions. The tandem rotor blades have different spanwise chord, camber, twist angle and inlet Mach number from 1.13 at the hub section to 1.48 at the tip section. 2D and 3D numerical simulations are carried out on the proposed design and the effect of each design parameter is examined. In depth analysis of the flow field is carried out at different operating conditions to explain the physical phenomena and the potential advantages.

2. Validation of the numerical model

Fig. 2 shows the geometry of the reference transonic rotor NASA Rotor 37. The rotor was originally designed and tested by Reid and Moore [14,15] at NASA Glenn research center alongside with three other stages named as stages 35, 36 and 38. The rotor consists of 36 blades with multiple circular arc airfoil sections. Each airfoil section has different chord, camber, thickness and setting angle. The rotor design parameters are summarized in Table 1.

NASA Rotor 37 was tested at Glenn research center by Suder [16] and the experimental results are used for numerical validation of several CFD codes and numerical models. AGARD advisory group conducted intensive numerical study to validate CFD codes and to identify the effect of grid and turbulence models on the solution accuracy [17]. The numerical method adopted in the current work is being motivated by the good results obtained for

Table 1
Rotor 37 design parameters.

Total pressure ratio	2.106
Total temperature ratio	1.27
Adiabatic efficiency	87.7%
Design mass flow rate [kg/s]	20.188
Rotor wheel speed [rpm]	17188.7
Rotor tip speed [m/s]	454.14
Rotor aspect ratio	1.19
Rotor solidity	1.29

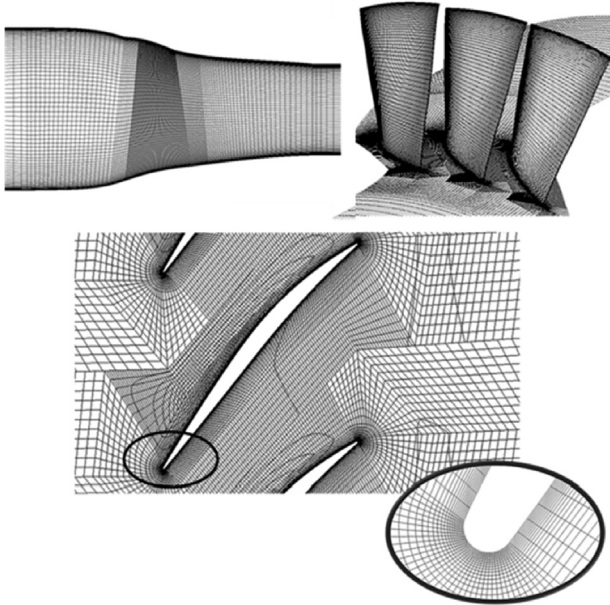


Fig. 3. The computational grid of Rotor 37.

NASA Rotor 37 in comparison with experimental data. The steady three-dimensional Reynolds Averaged Navier Stokes Equations are employed in the current study for the numerical simulations. The finite volume method is used for the numerical discretization of the governing equations. The one equation turbulence model of Spalart and Allmaras [18] is used for the turbulence calculation since it has shown good agreement with experimental data in AGARD report. It is designed for aerospace applications including wall bounded flows and it has shown very good results in boundary layers subjected to adverse pressure gradients and in turbomachinery applications. Also, it doesn't need large computational efforts.

The mesh is refined near the walls to ensure the wall y^+ to be around unity. To ensure highest numerical accuracy available for spatial discretization, second order upwind scheme is used for the turbulence equation while third order MUSCL scheme is used for flow discretization. The flow is assumed to be periodic in the azimuthal direction. Therefore, a sector of 10 degrees is considered as the computational domain. A 3D multi-block structured hexahedral mesh is generated for the rotor simulation as shown in Fig. 3.

Fig. 4 shows the computational domain and the boundary conditions. Moving reference frame model is employed to model the problem. Inlet boundary conditions are inferred from available experimental data [15]. Total pressure and temperature in the absolute frame of reference are applied at the inlet of the computational domain. Inlet flow is assumed to be axial according to the experimental data. Turbulence quantities at the inlet are defined in order to get 3% turbulence intensity at the inlet. A static pressure is imposed at the domain outlet and it is varied to get different flow rates and hence construct the compressor map. All walls are

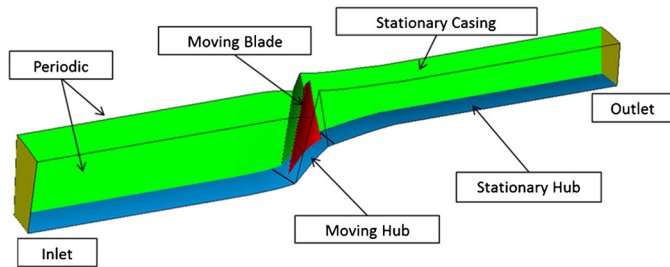


Fig. 4. Boundary conditions of the computational domain.

assumed to be adiabatic. The portion of the hub that is rotating with the blades is defined to be moving in the absolute reference frame and hence stationary in the rotating frame of reference. The casing is defined to be stationary in the absolute reference frame. Periodic boundary conditions are applied at the sides of the 10 degrees sector.

All flow properties are calculated at the same reference locations of the experimental data shown in Fig. 2. The rotor performance is expressed in terms of the total pressure ratio, total temperature ratio and the adiabatic efficiency. The rotor is simulated with three different grid sizes of 0.5 million, one million and two million hexahedral cells to check the numerical accuracy and the solution sensitivity to the grid. Radial distributions of the total pressure and total temperature ratios are plotted at station 4 against the experiment for the three grid sizes at 98% of the choking flow rate as illustrated in Fig. 5. All grids show quite good agreement with the experimental data. A grid independent solution is satisfied when the grid size is larger than one million cells since there is no significant difference between the results of 1 million and 2 million cells. The grid size is considered to be not less than 1 million cells in this current study.

The overall rotor performance map for both the CFD and the experiments is presented in Fig. 6. The numerical results are in good agreement with the experimental data at different rotor rotational speeds. The total pressure ratio is over predicted within 1%, while the rotor adiabatic efficiency is under predicted within 1.5%. Fig. 7 shows the relative Mach number contours at 70% of the blade span for 92.5% of the choking flow rate. The overall flow field, the lambda shock pattern and the flow separation associated with its interaction with the boundary layers is well captured in the numerical results.

In order to perform a parametric study on the tandem design of Rotor 37, two-dimensional numerical simulation is carried out at the mid-span section of Rotor 37, i.e. a slice in the circumferential direction, to show how far the isolated two-dimensional cascade is different from the full three-dimensional geometry. 2D rectilinear grid of the mid-span section is generated with 40,000 quadrilateral cells to ensure grid independent solution. The grid is refined near the airfoil walls to keep the value of y^+ close to 1. Translational periodicity is applied to mimic infinite cascade. The cascade is simulated in the relative frame of reference. The boundary conditions are obtained from the data provided by [14] for the mid-span section at design condition.

In order to check the validity and the accuracy of the two-dimensional simulations, the results are compared with those obtained from the three-dimensional simulations. Relative Mach number contours for both the two-dimensional cascade and the three-dimensional at mid-span are shown in Fig. 8. In addition, the static pressure distribution over the blade profile is presented in Fig. 9. The results of the two-dimensional simulations will be considered the reference for the tandem cascade design.

The passage shock pattern is predicted correctly. The shock position is slightly moved forward towards the airfoil leading edge

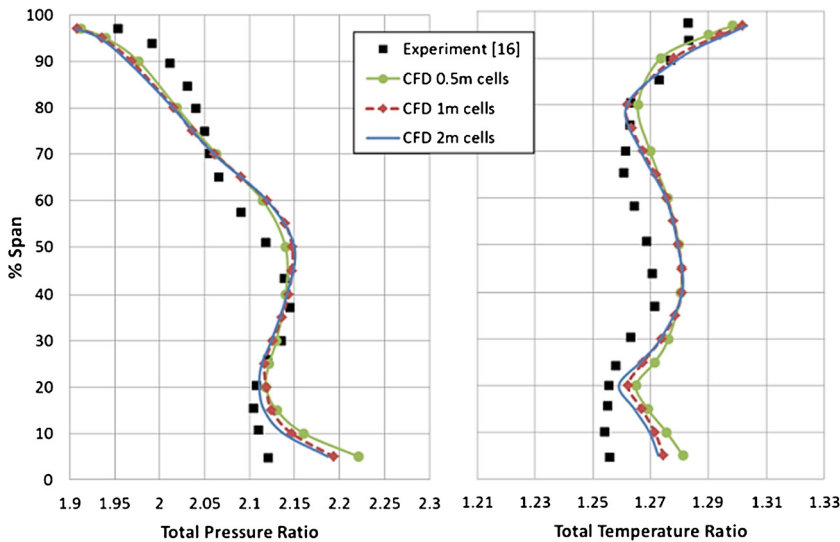


Fig. 5. Radial distributions at station 4 for the design speed and 98% of the choking flow rate.

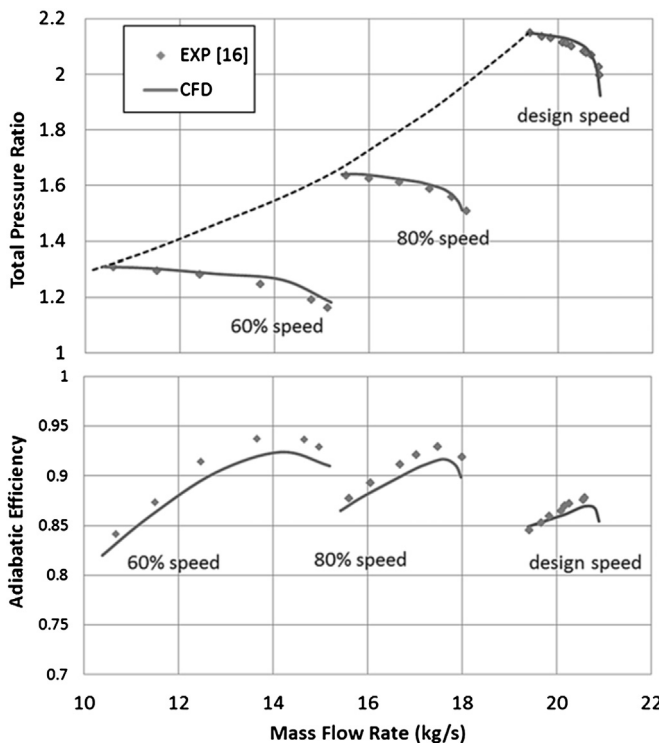


Fig. 6. Rotor37 performance map at different speed.

in the two-dimensional simulation and a larger separation zone is observed just behind the shock wave which may explain the under-estimation of the overall performance. This large separation zone is due to the slight difference in the inlet Mach number between the two-dimensional and three-dimensional cases, and adverse pressure gradient created due to the reduction in the axial velocity since the AVDR is unity for two-dimensional cascades. In conclusion, the two-dimensional simulation gives a good approximation of the flow behavior in the mid-span section. Thus, it is feasible to initially perform a parametric study on the tandem rotor in two-dimensional cascades. These results will be considered as an initial geometry for the three-dimensional simulations.

3. Two-dimensional parametric study for the transonic tandem cascades

3.1. Geometry and design parameters

A back of the envelope study has been carried out on a slotted blade to identify the effect of the loading split relative to the shock wave location on the overall cascade performance. It was concluded that the ideal loading split should take place just downstream of the shock wave location. The geometry description of the proposed tandem design is shown in Fig. 10. A 50 percent loading split is considered and the forward blade profile is kept the same as for the baseline single airfoil, while the aft airfoil profile and location are studied to obtain optimal cascade performance.

Two-dimensional rectilinear grids are generated for the proposed tandem designs as shown in Fig. 11. The inlet boundary conditions are kept similar to those used in the two-dimensional simulations of NASA Rotor 37 for the sake of comparisons. A parametric study is then carried out to identify the gap effect on the performance of the tandem cascade. The Axial Overlap Ratio (AOR) and the Tangential Overlap Ratio (TOR), shown in Fig. 10, are varied together resulting in a design matrix combination of different gap shapes. Some combinations are eliminated to avoid airfoils collision. The overall cascade performance is calculated in terms of the total pressure ratio, the adiabatic efficiency and the cascade diffusion factor variations with the loss coefficient which was defined by Lieblein et al. [19] as expressed by equations (4) and (5).

$$DF = 1 - \frac{W_2}{W_1} + \frac{C_{\theta 2} - C_{\theta 1}}{2\sigma W_1} \quad (4)$$

$$\omega = \frac{P_{t,rel1} - P_{t,rel2}}{P_{t,rel1} - P_1} \times \frac{\cos \beta_2}{2\sigma} \left(\frac{\cos \beta_2}{\cos \beta_1} \right)^2 \quad (5)$$

Fig. 12 shows the effect of various AOR and TOR combinations on the cascade total pressure ratio and efficiency. It is clear that the performance of the tandem cascade deteriorates when the gap between the forward and aft airfoils is too large. On the other hand, large improvement in the cascade performance is found when the two airfoils are close to each other. The peak performance occurs at the tandem design with (10% AOR–5% TOR) with 20% improvement in the cascade total pressure ratio and 5% improvement in the cascade adiabatic efficiency.

Mach number contours for the baseline single airfoil cascade and the (10% AOR–5% TOR) tandem cascade are presented in

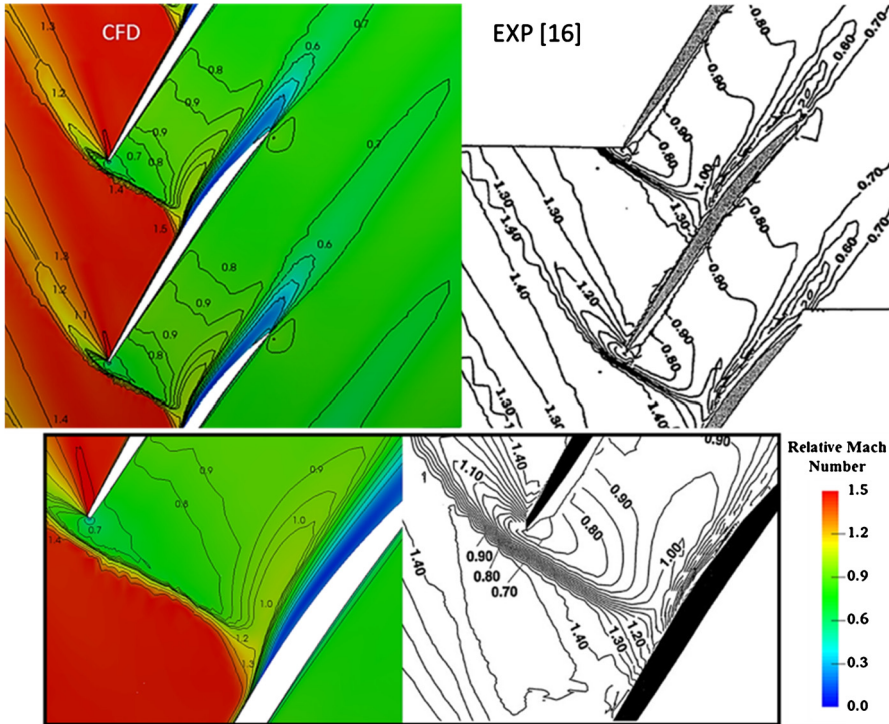


Fig. 7. Relative Mach number contours at 92.5% chocking flow rate at design speed for 70% span.

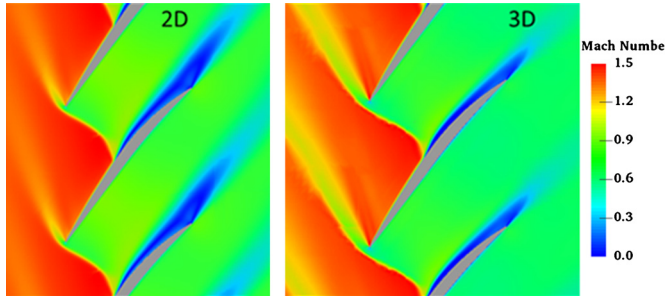


Fig. 8. Mach number contours for the 2D cascade simulation (left) and the 3D rotor simulation at 50% span (right).

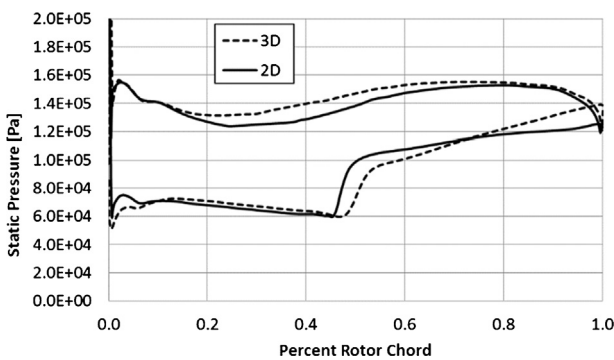


Fig. 9. Static pressure distribution over the airfoil length for 2D and 3D simulations.

Fig. 13. The flow field and the shock pattern on the forward airfoil suction surface are similar in the two cases since the flow is supersonic and it is not affected by the changes downstream. It is evident that the gap flow creates a fresh boundary layer and attaches the flow to the aft airfoil suction surface resulting in diminishing the separation zone in the rear half of the cascade. The more utilization of the cascade passage area increases the diffusing action. Thus, the reduction in the velocity in the cascade frame

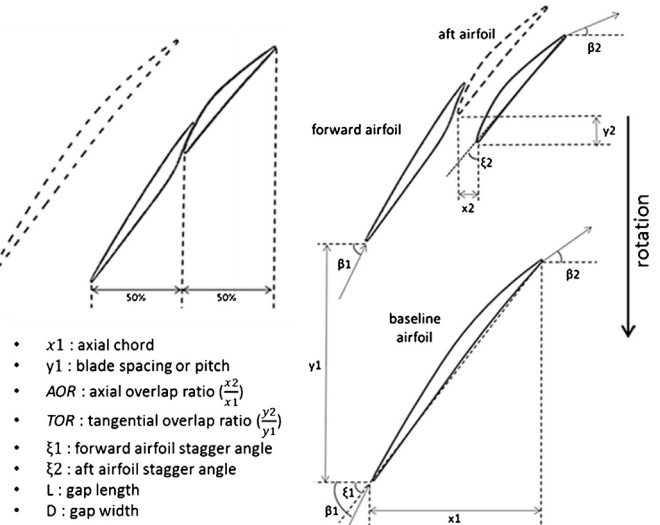


Fig. 10. Tandem blade geometry description.

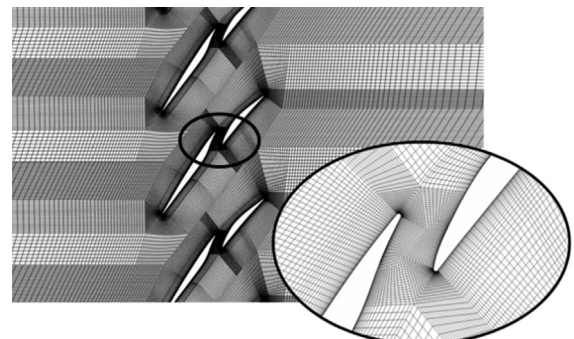


Fig. 11. Computational grid for 2D tandem cascades.

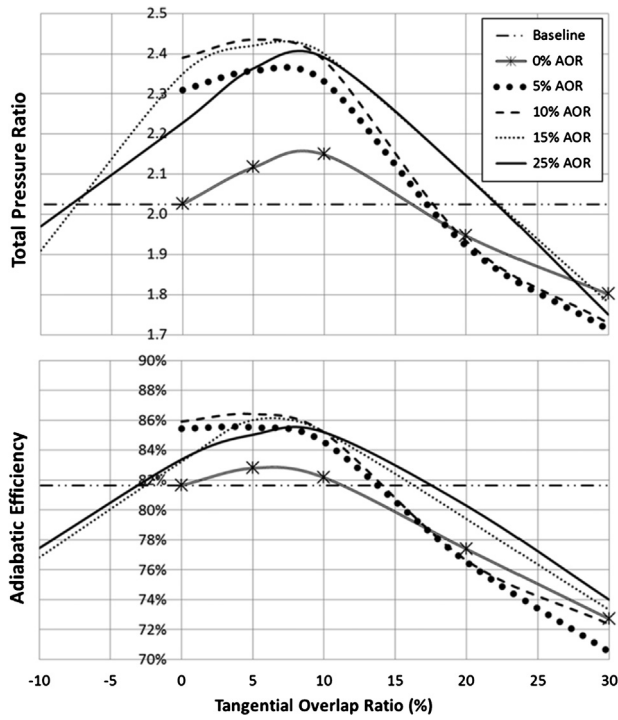


Fig. 12. Cascade performance with different AOR and TOR.

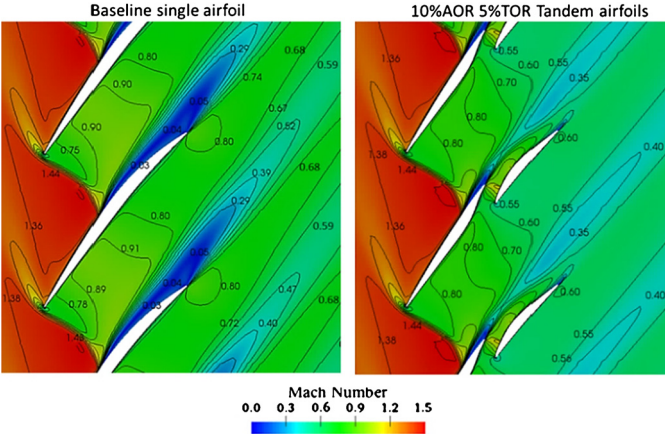


Fig. 13. Mach number contours for the baseline and tandem airfoils.

of reference is transformed to a static pressure rise as illustrated in the static pressure contours in Fig. 14.

The static pressure distribution over the airfoil surface versus the axial chord is plotted in Fig. 15. The forward airfoil pressure side loading is increased due to the induced flow circulation resulting from the interaction with the aft airfoil. The loading of the aft airfoil is increased compared to the rear half of the baseline airfoil resulting in a large improvement in the overall cascade performance.

3.2. Tandem cascade of 10% AOR and different TOR

To understand the physics behind the variation of the performance with the relative position between the forward and aft airfoils, the cascade losses for 10% AOR with different TOR is introduced as the dashed curve in Fig. 12. The results are compared with the baseline Rotor 37 mid-span cascade on Lieblein's chart as shown in Fig. 16. The tandem cascades with large gap between the forward and aft airfoil represented by the two points of 30% TOR and 20% TOR have higher losses than the baseline cascade with

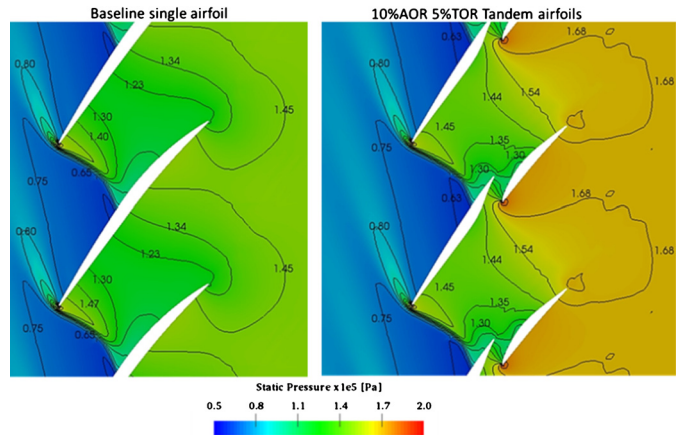


Fig. 14. Static pressure contours for the baseline and tandem airfoils.

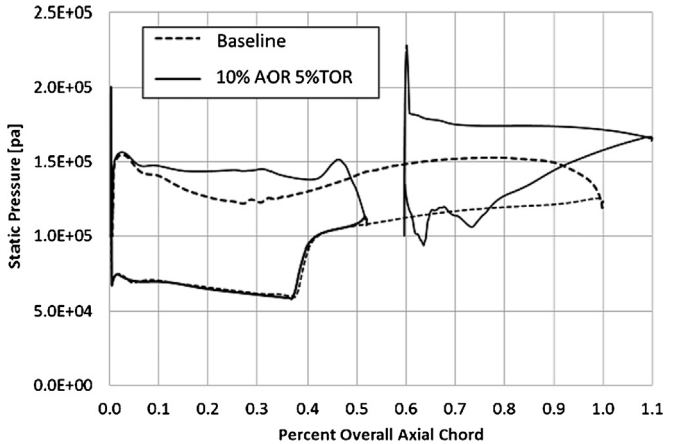


Fig. 15. Surface static pressure distribution.

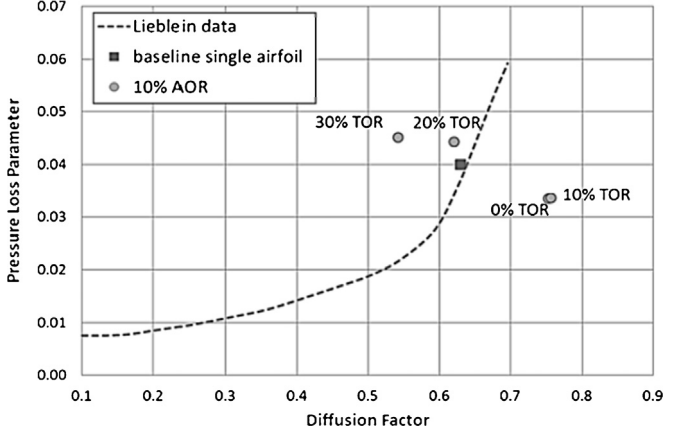


Fig. 16. Cascade losses for 10% AOR with different TOR.

less diffusion. While the tandem cascades with small gap represented by the two points 0% and 10% TOR have higher diffusion with smaller losses compared to the baseline cascade.

Mach number contours for the selected cases are plotted in Fig. 17. The flow pattern over the aft airfoil is quite similar in the cases with 0% and 10% TOR. However, more flow diffusion is achieved in the 10% TOR case which can be observed in lower Mach number contours behind the rotor. Also a larger low speed zone is extended from the forward airfoil trailing edge due to the split between the main flow stream and the gap flow attached and turning with the aft airfoil suction side.

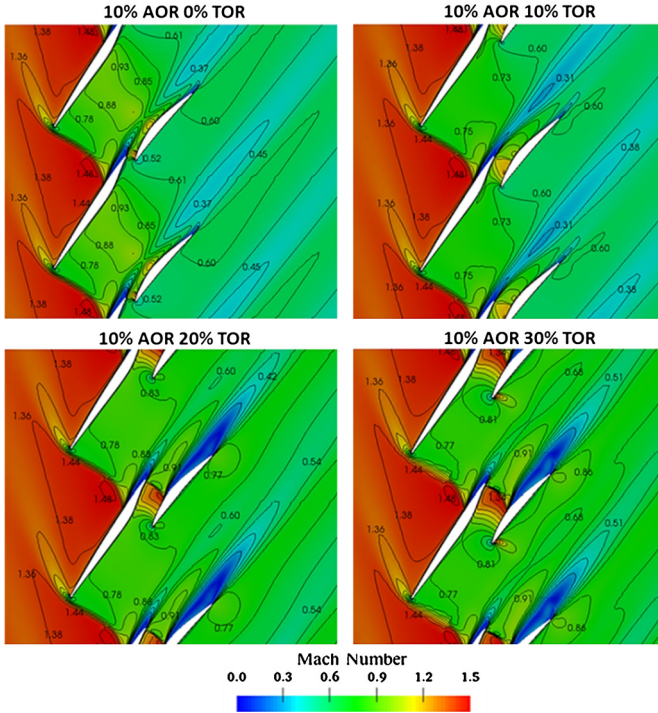


Fig. 17. Mach number contours for 10% AOR with different TOR.

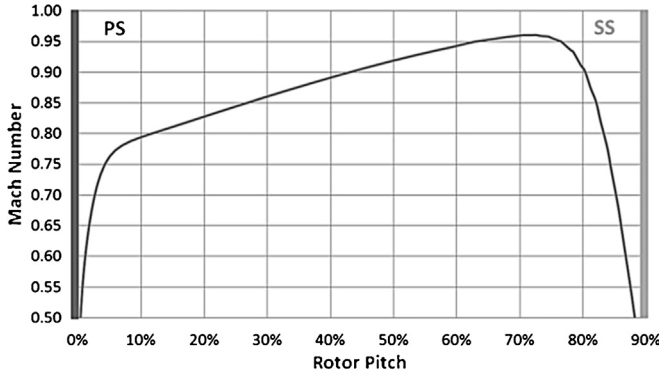


Fig. 18. Pitch-wise distribution of the Mach number.

The aft airfoil in the cases with large TOR is subjected to higher inlet Mach number than the cases with low TOR since the flow acceleration is large near the blade suction side and low near the blade pressure side as shown in Fig. 18. Thus, the flow acceleration on the aft airfoil suction surface increases in the cases with 20% and 30% TOR. A shock wave with 1.4 upstream Mach number is created causing the flow to separate from the aft airfoil suction surface due to its interaction with the boundary layer [20].

The gap tends to guide the flow from the high pressure region to the low pressure region, i.e. from the pressure side of the forward airfoil to the suction side of the aft airfoil, thus increasing the aft airfoil incidence angle. However this effect diminishes for large gap areas, i.e. large TOR and results into decreasing the aft airfoil incidence angle as shown in Fig. 19. This may explain the small flow acceleration in the case of 30% TOR case as shown in Fig. 17 at the aft airfoil pressure surface near its leading edge.

3.3. Tandem cascade of 0% AOR and different TOR

Fig. 20 shows the Mach number contours for selected cases with 0% AOR at different TOR, represented by the starred curve in Fig. 12 which has the lowest performance. It is evident that the

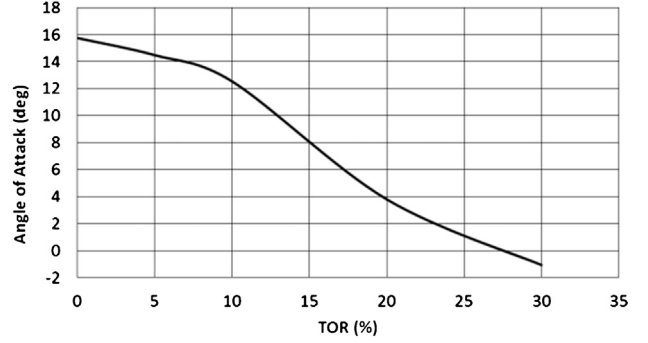


Fig. 19. Aft airfoil incidence angle variation with TOR.

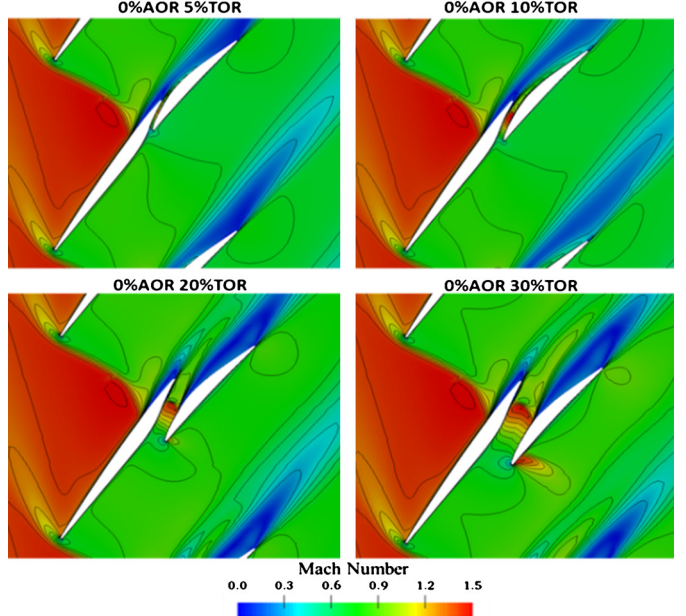


Fig. 20. Mach number contours for 0% AOR with different TOR.

gap flow is very small in the 5% and 10% TOR cases such that it fails to clean the separated flow properly. On the other hand, the 20% and 30% TOR cases have the problem of high aft airfoil inlet Mach number and negative incidence angle as explained in the previous section.

3.4. Tandem cascades of different AOR and 5% TOR

Fig. 21 shows the Mach number contours for selected cases with different AOR at 5% TOR, which represent a vertical line in Fig. 12. The variation in the cascade performance is minimal with the change in the axial direction. This is due to the slight variation in the aft airfoil inlet Mach number and incidence angle with the axial direction. It is important to note that the increase in the axial overlap ratio is unfavorable since it means an increase in the rotor disc length and the overall compressor weight, while the basic objective of tandem rotors is to reduce the compressor weight by reducing the number of rotor discs as much as possible.

3.5. Aft airfoil shape optimization

To study the effect of increasing the turning and diffusion of the aft airfoil on the flow field of the tandem cascade, an optimization process is carried out to produce the aft airfoil profile which gives the maximum pressure rise in the cascade. The MMO (Mesh Morphing Optimizer) [21], an embedded module in the CFD solver, is

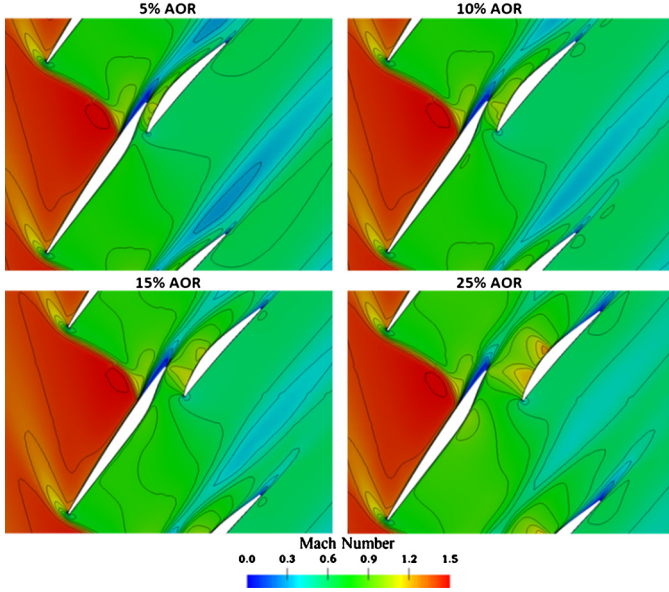


Fig. 21. Mach number contours for different AOR at 5% TOR.

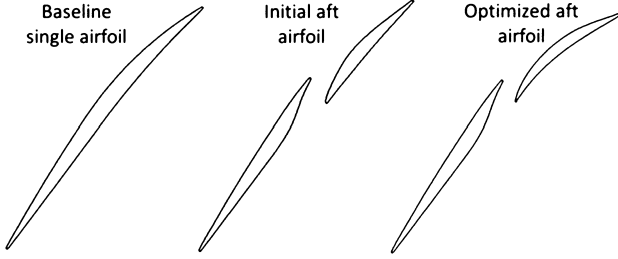


Fig. 22. Aft airfoil profile.

used in the optimization process. This module has the advantage of morphing the grid to get multiple geometries instead of creating a new geometry and grid in each stage in the optimization process.

Ten moving control points are defined with two optimization parameters for each, horizontal displacement and vertical displacement. The cascade total pressure ratio is defined as the objective function to be maximized and the SIMPLEX optimization algorithm is used to perform the function optimization. The (10% AOR–5% TOR) tandem cascade is taken as a reference in the aft airfoil optimization process, i.e. the aft airfoil position is conserved in the optimization process, and only the aft airfoil profile is changed. Fig. 22 shows the aft airfoil before and after optimization.

Further improvement in the cascade total pressure ratio is achieved with the optimized aft airfoil as seen in the static pressure distribution over the airfoil surface in Fig. 23. The loading of the forward airfoil pressure side increased slightly near the trailing edge due to the interaction with the optimized aft airfoil. The pressure distribution on the optimized aft airfoil increased significantly on the pressure surface resulting in higher loading on the aft airfoil.

A diffusion factor of 0.89 is achieved as indicated in Fig. 24. However, the cascade losses increase for the optimized aft airfoil because of the enlarged low speed region formed in the wake of the forward airfoil. In this region the Mach number dropped from 0.35 in the initial aft airfoil to 0.18 in the optimized aft airfoil as illustrated in Fig. 25. Fig. 26 is the velocity vectors for the two cases showing the blockage region, bounded by the dashed line, which is formed between the main flow stream from the forward airfoil and the highly turning flow on the aft airfoil through the tandem gap. This enlarged zone may cause non-uniformity in the inflow to the

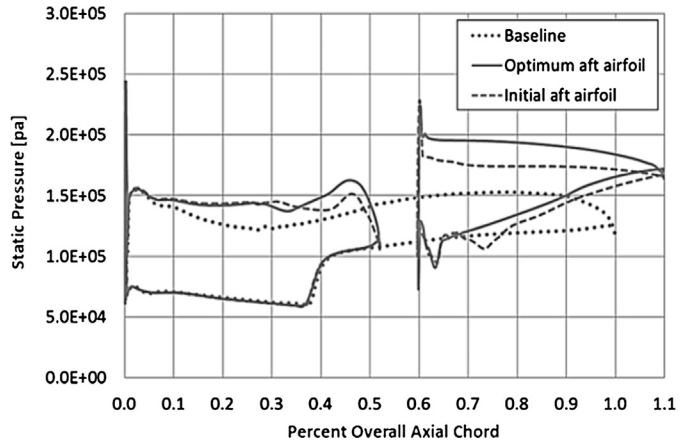


Fig. 23. Static pressure distribution over axial chord for the optimized aft airfoil.

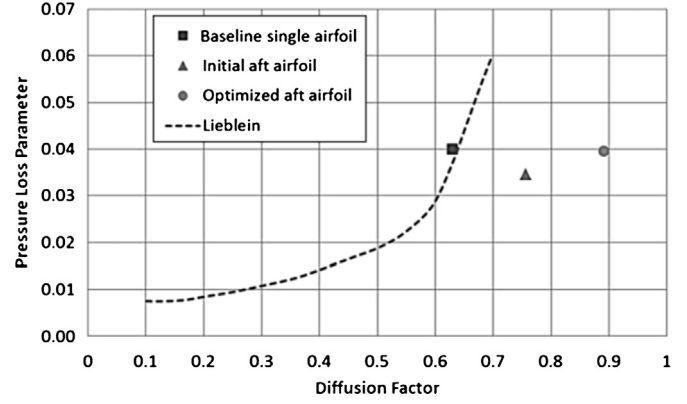


Fig. 24. Cascade losses for the initial and the optimized aft airfoils.

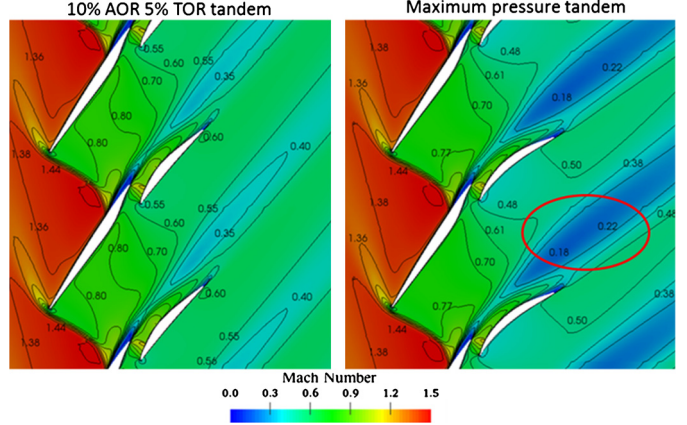


Fig. 25. Mach number contours for initial and optimized aft airfoils.

following stator guide vane. Thus, there should be a compromise between the flow turning and the uniformity of the exit profile.

4. 3D Transonic tandem rotor performance

The three-dimensional numerical simulations of tandem rotor are performed starting from the geometry obtained with two-dimensional study. The performance of the tandem rotor at the design and off-design conditions is investigated. Recall that the reference baseline NASA Rotor 37 has variable airfoil chord, thickness and stagger angle for each section in the radial direction. As in the 2D study, to keep the inflow characteristics the same, the forward airfoil shape for each radial section is kept similar to the reference

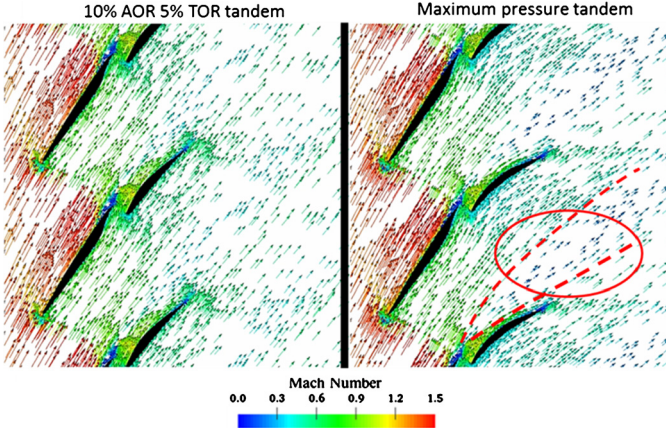


Fig. 26. Velocity vectors for initial and optimized aft airfoils.

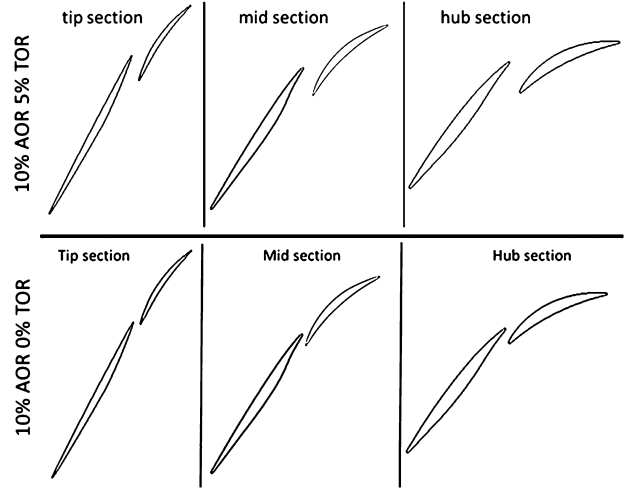


Fig. 28. Blade sections for two different tandem designs.

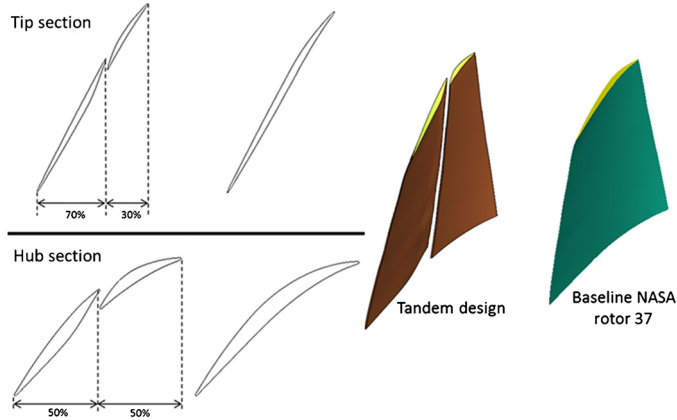


Fig. 27. 3D tandem loading split.

NASA rotor 37 and the forward 3D blade is constructed from different profiles in the radial direction.

Since the passage shock moves towards the trailing edge near the tip section, the tandem split is carried out at 50% of the axial chord for the hub section to avoid the interaction between the passage shock wave and the tandem gap. The position of the split is then varied linearly with the blade span such that the split takes place at 70% of the axial chord for the tip section as illustrated in Fig. 27.

The aft airfoil obtained from the two dimensional optimization for maximum total pressure ratio at mid-span section is scaled with the chord and thickness ratio of each radial section. It is then placed at two different locations relative to the forward airfoil to construct two different 3D tandem rotor blades one with (10% AOR-5% TOR) and another with (10% AOR-0% TOR) as shown in Fig. 28.

Three dimensional numerical simulations are carried out on the multi-block structured hexahedral mesh of tandem rotors as shown in Fig. 29. For the sake of comparison, the computational model, including flow path, tip clearance, boundary conditions and numerical settings, is kept similar to the model used in the numerical simulation of the reference NASA rotor 37.

The back pressure is increased with certain interval to vary the mass flow rate and hence construct the compressor performance map. Fig. 30 shows the total pressure ratio for the baseline NASA rotor 37 and the two tandem rotors at the design speed. A significant rise in the total pressure ratio is achieved in both the tandem rotors. However, unconverted solutions are obtained for mass flow rates less than 20.35 kg/s for the tandem rotor with (10% AOR-5% TOR) which is an indicator of a surge or stalling phenomena in

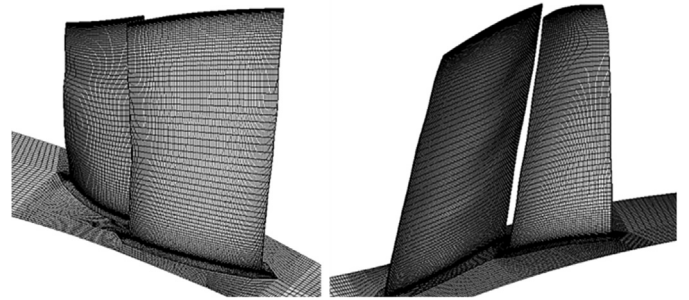


Fig. 29. Computational grid for the 3D tandem rotor, looking at suction side (left), looking at pressure side (right).

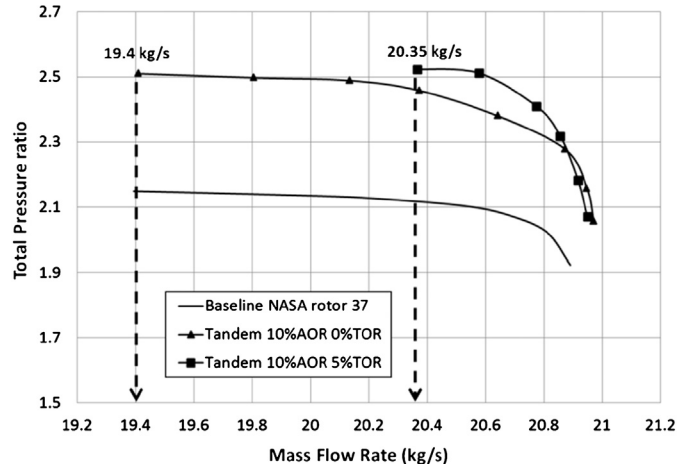


Fig. 30. Performance of the 3D tandem rotors at design speed.

the tandem rotor. However, both the baseline NASA rotor 37 and the (10% AOR-0% TOR) tandem rotor were found to stall almost at the same flow rate of 19.4 kg/s.

The stall mechanism of the reference rotor (NASA rotor 37) starts from the tip section and it is primarily due to the interaction between the blade tip vortex and the passage shock. It is dependent upon the inflow characteristics i.e. the inlet flow angle and the Mach number [22–24]. Since the inflow characteristics and the forward blade geometry of the tandem rotor are similar to the baseline rotor, thus the narrow stability range of the (10% AOR-5% TOR) tandem rotor must be due to the introduction of the aft blade.

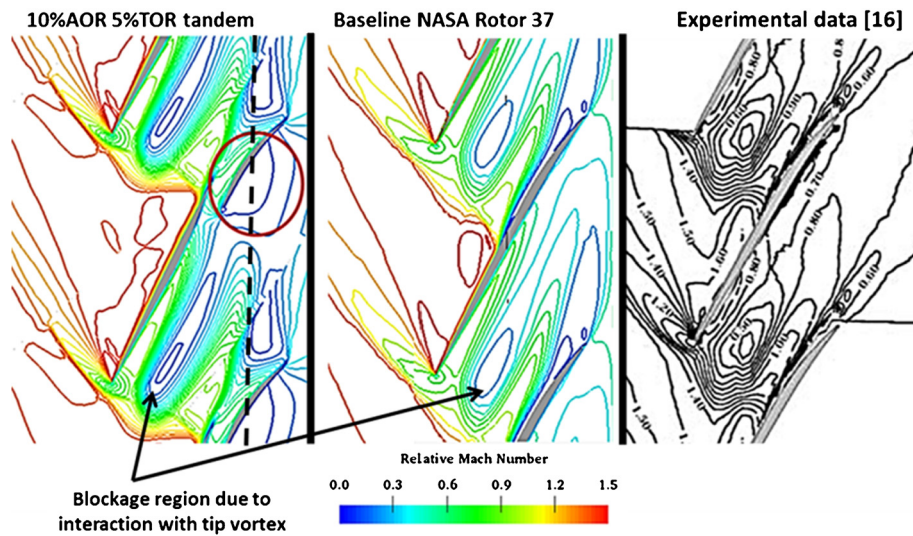


Fig. 31. Relative Mach number contours near stall at 95% span.

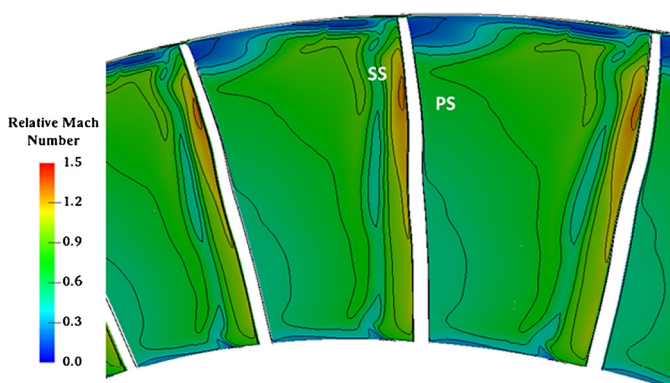


Fig. 32. Relative Mach number contours in the axial direction at the aft airfoil mid-chord (dashed line in Fig. 31).

The relative Mach number contours at 95% span near stalling flow rate obtained using the numerical simulations for both the baseline NASA rotor 37 and the (10% AOR-5% TOR) tandem rotor are compared with those obtained from experiments as shown in Fig. 31. The blockage region due to the interaction between the tip vortex and the passage shock exists in the both reference and tandem rotors. However, there exists another blockage region near the aft airfoil pressure side, bounded by the circle, and extends downstream in the pitch-wise direction as indicated in Fig. 32.

Fig. 33 shows the aft airfoil incidence angle distribution with the span-wise direction for the (10% AOR-0% TOR) and the (10% AOR-5% TOR) tandem rotors. The aft airfoil at the tip section of the (10% AOR-5% TOR) tandem rotor has a negative incidence angle which causes the flow to separate from the pressure side. This agrees with the concluded remarks from the 2D parametric study that placing the aft airfoil at high TOR reduces its incidence angle.

To get a compromised design between the 0% TOR and 10% TOR tandem rotors, the aft airfoil position is linearly varied in the radial direction such that the TOR is 10% for hub section and 0% for tip section. The tandem rotor is simulated at different rotor rotational speeds to examine its performance at subsonic other than supersonic inlet conditions. Fig. 34 shows the performance map of the tandem rotor compared to the baseline single airfoil NASA rotor 37 at different operating speeds. The variable TOR tandem rotor

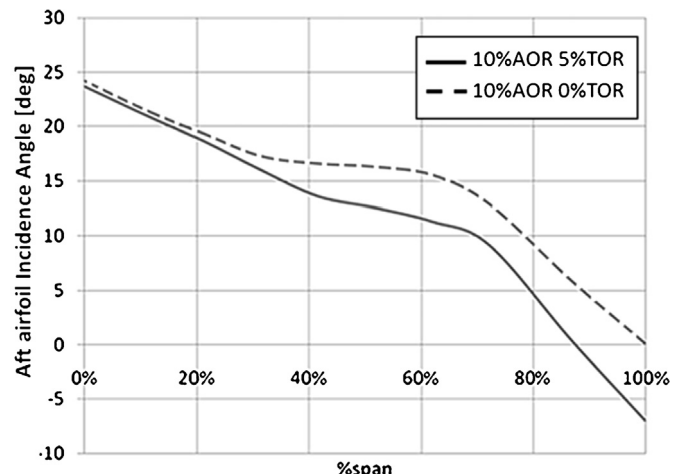


Fig. 33. Variation of the aft airfoil incidence angle with the blade span.

Table 2
Performance summary at design point (20.2 kg/s).

Case	Total pressure ratio	Total temperature ratio	Adiabatic efficiency
Rotor 37 (EXP)	2.106	1.27	87.7%
Rotor 37(CFD)	2.127	1.28	86.3%
Tandem (CFD)	2.495 (17%)	1.34	88.6%

achieved 17% increase in the total pressure ratio and 2% improvement in the adiabatic efficiency at the design flow rate of 20.2 kg/s. The rotor performance is summarized in Table 2.

A comparison between the flow field at the design flow rate in the 3D tandem rotor and the baseline “NASA rotor 37” at different spanwise locations is represented in terms of the relative Mach number contours as shown in Fig. 35 through 37. The flow field in the tandem rotor shows the advantage of cleaning the separation region behind the shock wave and flow higher diffusion. However, some low velocity regions appears in the wake of the forward blade due to the large flow turning as explained earlier in this paper.

Fig. 38 shows the mid-span relative Mach number contours at 92.5% of the choking flow rate (near stall). The shock wave is pushed forward towards the rotor inlet and the separation zone increase in the baseline NASA rotor 37. The flow pattern is still

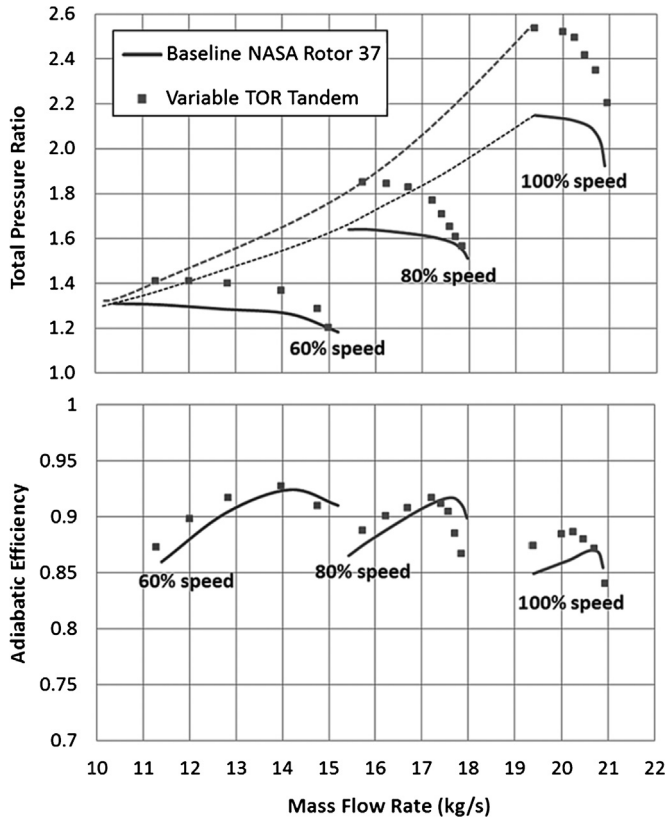


Fig. 34. Tandem rotor performance map.

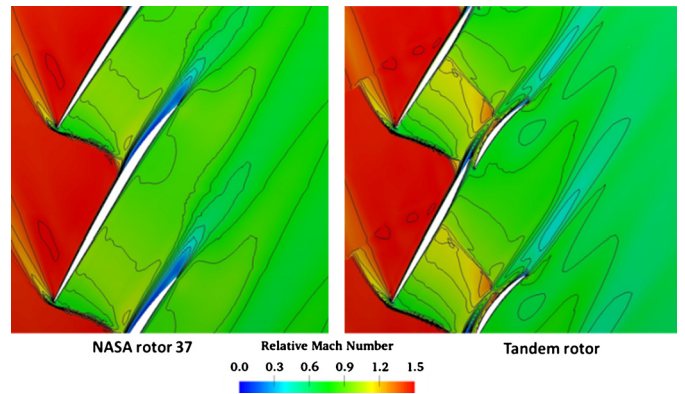


Fig. 37. Relative Mach number contours at design flow, 80% span.

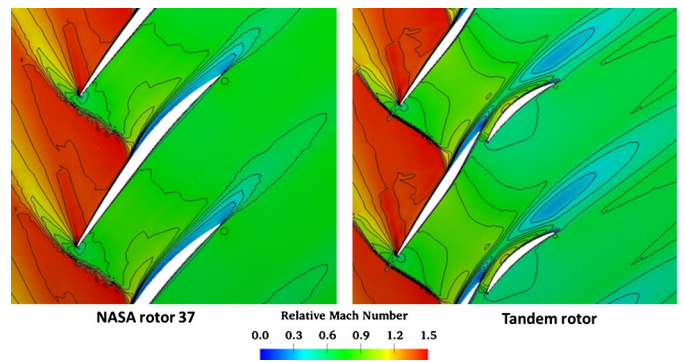


Fig. 38. Relative Mach number contours near stall, 50% span.

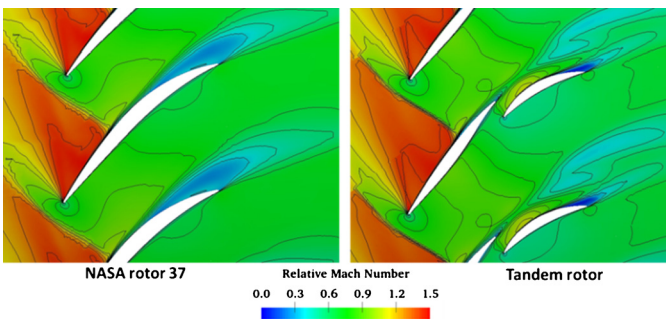


Fig. 35. Relative Mach number contours at design flow, 20% span.

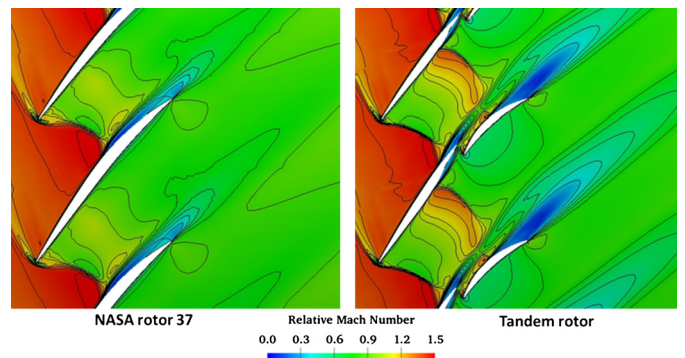


Fig. 39. Relative Mach number contours near choking, 50% span.

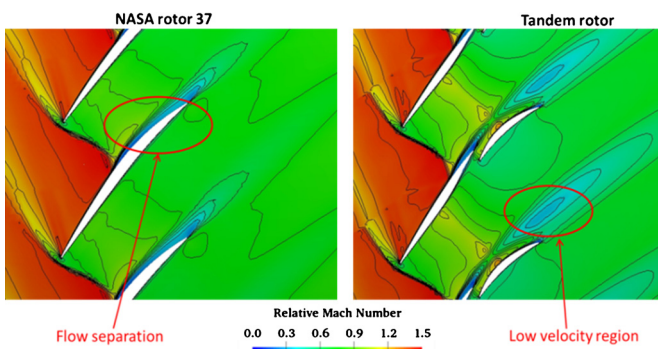


Fig. 36. Relative Mach number contours at design flow, 50% span.

showing advantage of the tandem rotor in terms of reducing the separation zone and increasing the flow diffusion.

On the other hand, the flow field near the rotor choking, shown in terms of the relative Mach number contours in Fig. 39, shows disadvantage of the tandem rotor. The shock wave is pushed far downstream in the passage towards the rotor exit. The inlet Mach number to the aft airfoil increases and a second shock wave is formed on its suction side causing the flow to separate. This may explain the reduction in the adiabatic efficiency near the rotor choking.

Fig. 40 shows the relative Mach number contours at 50% span for 60% rotational speed in which the inlet Mach number is subsonic. No shock waves exist in the flow passage. The tandem design is still showing advantage of higher flow diffusion on the aft airfoil which is translated into a rise in the rotor total pressure ratio.

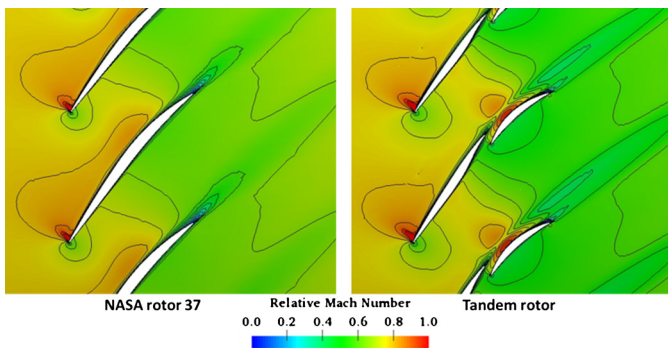


Fig. 40. Relative Mach number contours at 60% speed near peak efficiency, 50% span.

5. Conclusions

A proposed design of the transonic tandem rotor is introduced with same inflow characteristics of the reference NASA rotor 37. The forward airfoil shape is kept the same as in NASA rotor 37 while the aft airfoil profile and location are changed to identify the effect of each design parameter on the tandem rotor performance. Two-dimensional parametric study is considered at the design flow rate, and then the computations are extended to three-dimensional domain.

The two-dimensional tandem parametric study shows that large improvement in the cascade total pressure ratio with slight improvement in the adiabatic efficiency could be achieved when the aft airfoil is close to the forward airfoil in the pitch wise direction. The effect of the AOR is found to be minimal. It is concluded that placing the aft airfoil at a large distance in the pitch wise direction decreases the aft airfoil incidence angle and increases its inlet Mach number. This results in existence of a shock wave on the aft airfoil suction surface which tends the flow to separate resulting in deterioration of the overall cascade performance. On the other hand, the cases with negative AOR, which represent a small gap area, could not clean the separated zone properly due to low flow rate from the forward airfoil pressure surface to the aft airfoil suction surface.

Further improvement in the flow turning and diffusion is achieved by optimizing the aft airfoil profile, however large flow turning could lead to the existence of large low velocity regions in the wake of the forward airfoil due to splitting the flow into the main stream and highly turning gap flow. This region may affect the uniformity of the inflow to the next stator.

Finally, 3D tandem rotors are constructed and numerical simulation is carried out to compare the performance with that of the baseline NASA rotor 37 at different operating conditions. It was found that the TOR has to be reduced as getting close to the tip section to avoid tip stall due to aft airfoil negative incidence angle. The tandem rotor with variable TOR performed well at design and off design conditions. 17% increase in the total pressure ratio with 2% improvement in the adiabatic efficiency was achieved at design flow rate.

Conflict of interest statement

The authors declare that there is no actual or potential conflict of interest including any financial, personal or other relationships with other people or organizations that could inappropriately influence, or be perceived to influence, their work.

References

- [1] A.J. Wennerstrom, Highly loaded axial flow compressors: history and current developments, *J. Turbomach.* 112 (1990) 567–578.
- [2] R. Biollo, E. Benini, Recent advances in transonic axial compressor aerodynamics, *Prog. Aerosp. Sci.* 56 (2013) 1–18.
- [3] J.W. Raily, M.E. El-Sarha, An investigation of the flow through tandem cascades, *Proc. Inst. Mech. Eng.* 180 (1965) 66–73.
- [4] J.A. Brent, D.R. Clemons, Single-Stage Experimental Evaluation of Tandem-Airfoil Rotor and Stator Blading for Compressors, NASA Contract Report 134713, 1974.
- [5] U.K. Saha, B. Roy, Experimental investigations on tandem compressor cascade performance at low speeds, *Exp. Therm. Fluid Sci.* 14 (1997) 263–276.
- [6] K. Bammert, H. Beelte, Investigation of an axial flow compressor with tandem cascades, *J. Eng. Power* 102 (1980) 971–977.
- [7] J. McGlumphy, W. Ng, S. Wellborn, S. Kempf, 3D numerical investigation of tandem airfoils for a core compressor rotor, *J. Turbomach.* 132 (2010) 31009.
- [8] J. McGlumphy, W.-F. Ng, S.R. Wellborn, S. Kempf, Numerical investigation of tandem airfoils for subsonic axial-flow compressor blades, *J. Turbomach.* 131 (2009) 21018.
- [9] M. Hoeger, R.-D. Baier, S. Fischer, J. Neudorfer, High Turning Compressor Tandem Cascade for High Subsonic Flows – Part 1: Numerical and Experimental Investigations, *AIAA paper 2011-5601*, 2011.
- [10] M. Hoeger, R.-D. Baier, S. Fischer, J. Neudorfer, High Turning Compressor Tandem Cascade for High Subsonic Flows – Part 2: Numerical and Experimental Investigations, *AIAA paper 2011-5602*, 2011.
- [11] H. Hasegawa, A. Matsuoka, S. Suga, Development of Highly Loaded Fan with Tandem Cascade, *AIAA paper 1065*, 2003.
- [12] A. Weber, W. Stelnert, Design, Optimization, and Analysis of a High-Turning Transonic Tandem Compressor Cascade, *ASME paper 97-GT-412*, 1997.
- [13] L. Qiushi, W. Hong, Z. Sheng, Application of tandem cascade to design of fan stator with supersonic inflow, *Chin. J. Aeronaut.* 23 (2010) 9–14.
- [14] R.D. Reid, L. Moore, Design and Overall Performance of Four Highly Loaded, High-Speed Inlet Stages for an Advanced High-Pressure Ratio Core Compressor, *NASA Technical Paper 1337*, 1978.
- [15] L. Reid, Performance of Single Stage Transonic AFC Rotor and Stator Aspect Ratio of 1.19 and 1.26, Resp. and with Design Pressure Ratio of 2.05, *NASA Technical Paper 1659*, 1980.
- [16] K.L. Suder, Experimental Investigation of the Flow Field in a Transonic, Axial Flow Compressor with Respect to the Development of Blockage and Loss, *NASA Technical Memorandum 107310*, 1996.
- [17] J. Dunham, CFD Validation for Propulsion System, *AGARD-AR-335*, 1998.
- [18] P.R. Spalart, S.R. Allmaras, J. Reno, A One-Equation Turbulence Model for Aerodynamic Flows, *AIAA paper 1992-0439*, 1992.
- [19] S. Lieblein, F. Schwenk, R. Broderick, Diffusion Factor for Estimating Losses and Limiting Blade Loading in Axial Flow Compressor Blade Elements, *NACA Research Memorandum E53D01*, 1953.
- [20] J. Seddon, The Flow Produced by Interaction of a Turbulent Boundary Layer with a Normal Shock Wave of Strength Sufficient to Cause Separation, *British Aero. Res. Council Reports and Memo 3502*, 1960.
- [21] ANSYS Inc, *ANSYS Fluent User's Guide*, 2013.
- [22] K.L. Suder, M.L. Celestina, Experimental and computational investigation of the tip clearance flow in a transonic axial compressor rotor, *J. Turbomach.* 118 (1996) 218–229.
- [23] R.V. Chima, Calculation of tip clearance effects in a transonic compressor rotor, *J. Turbomach.* 120 (1998) 131–140.
- [24] K. Yamada, K. Funazaki, M. Furukawa, The Behavior of Tip Clearance Flow at Near-Stall Condition in a Transonic Axial Compressor Rotor, *ASME paper GT2007-27725*, 2007.